J Mater Sci (2013) 48:2934–2952
DOI 10.1007/s10853-012-6968-z

ENERGY MATERIALS & THERMOELECTRICS

The influence of constrictivity on the effective transport properties of porous layers in electrolysis and fuel cells

L. Holzer · D. Wiedenmann · B. Münch · L. Keller · M. Prestat · Ph. Gasser · I. Robertson · B. Grobéty

Received: 11 May 2012 / Accepted: 15 October 2012 / Published online: 26 October 2012

Abstract The aim of the present investigation is to define microstructure parameters, which control the effective transport properties in porous materials for energy technology. Recent improvements in 3D-imaging (FIB-nanotomography, synchrotron X-ray tomography) and image analysis (skeletonization and graph analysis, transport simulations) open new possibilities for the study of microstructure effects. In this study, we describe novel procedures for a quantitative analysis of constrictivity, which characterizes the so-called bottleneck effect. In a first experimental part, methodological tests are performed using a porous (La,Sr)CoO_3 material (SOFC cathode). The tests indicate that the proposed procedure for quantitative analysis of constrictivity gives reproducible results even for samples with inhomogeneous microstructures (cracks, gradient of porosity). In the second part, 3D analyses are combined with measurements of ionic conductivity by impedance spectroscopy. The investigations are preformed on membranes of electrolysis cells with porosities between 0.27 and 0.8. Surprisingly, the tortuosities remain nearly constant (1.6) for the entire range of porosity. In contrast, the constrictivities vary strongly and correlate well with the measured transport resistances. Hence, constrictivity represents the dominant microstructure parameter, which controls the effective transport properties in the analysed membrane materials. An empirical relationship is then derived for the calculation of effective transport properties based on phase volume fraction, tortuosity, and constrictivity.

L. Holzer (✉) · L. Keller
Institute of Computational Physics ICP, ZHAW, Zurich University of Applied Sciences, Wildbachstrasse 21, 8400 Winterthur, Switzerland
e-mail: holz@zhaw.ch

D. Wiedenmann · B. Grobéty
Department of Geosciences and FRIMAT, University of Fribourg, Chemin du Musée 6, Pérolles, 1700 Fribourg, Switzerland

D. Wiedenmann · B. Münch · M. Prestat · I. Robertson
EMPA, Swiss Federal Laboratories for Materials Testing and Research, Überlandstrasse 129, 8600 Dübendorf, Switzerland

M. Prestat · Ph. Gasser
ETHZ, Swiss Federal Institute of Technology Zürich, Wolfgang-Pauli-Str. 10, 8093 Zurich, Switzerland

I. Robertson
School of Chemistry, University of St. Andrews, North Haugh, St. Andrews KY16 9ST, UK

Abbreviations

β	Constriction factor (r^2_{min}/r^2_{max})
$\beta_{Petersen}$	Constriction factor from Petersen [30], $=1/\beta$
δ	Constrictivity
δ_{geo}	Geometric constrictivity, determined via constriction factor (β) and using Eq. 9
Δ	Oxygen deficiency in the perovskite crystal lattice
ε	Porosity
ϕ	Wetting angle
γ	Surface tension in Eq. 7
γ	Quadratic function of β in Eq. 10
σ_{eff}	Effective conductivity
σ_0	Intrinsic conductivity of K(OH)-solution
σ_r	Relative conductivity (σ_{eff}/σ_0)
τ_{exp}	Experimental tortuosity, indirectly determined
τ_{elc}	Electrical tortuosity, indirectly determined using EIS data
τ_{geo}	Geometric tortuosity, directly measured from tomographs
µm	Micrometre

A_{max}	Cross section of pore at 'non-constricted' bulges and/or at pore entrance
A_{min}	Cross section of pore at bottleneck (constriction)
c-PSD	Continuous-pore size distribution
d-PSD	Discrete-pore size distribution
D_{eff}	Effective diffusivity
D_0	Intrinsic diffusivity
EIS	Electrical impedance spectroscopy
F	Formation factor
FIB	Focused ion beam
ID_{crit}	Critical intrusion depth
LSC	(La,Sr)$CoO_{3-\Delta}$/perovskite/SOFC cathode material
m	Empirical exponential factor with basis e (Archie's law)
MIP	Mercury intrusion porosimetry
MIP-PSD	Pore size distribution from (simulation of) mercury intrusion porosimetry
P_c	Capillary pressure
R_c	Capillary radius
r_{max}	Radius of pore at pore entrance and at 'non-constricted' bulges
r_{min}	Radius of pore at bottleneck (constriction)
R_{eff}	Effective resistivity to ion conduction of a porous membrane filled with electrolyte
R_0	Intrinsic resistivity of electrolyte
SRμCT	Synchrotron radiation microcomputed tomography
SOFC	Solid oxide fuel cell

Introduction

This article deals with the question of whether the effect of microstructural features on the macroscopic transport properties can be described by means of a few volume-averaged parameters such as porosity, tortuosity and constrictivity. This question was discussed vividly throughout the twentieth century in numerous research disciplines such as geoscience, chemical engineering and materials science [1–6], without being conclusive. Today, the recent progress in nanotomography and 3D image analysis provides new experimental results, which shed more light on the old discussion about microstructure and its influence on the effective transport properties.

Two groups of research disciplines are distinguished here where transport properties are of particular interest. The first group considers transport by diffusion or flow in porous media (e.g. rocks, soils, porous engineering materials, membranes, filters, cement and concrete, wood, etc.). This kind of research is related to some economically important topics such as for example the exploitation of gas and oil from porous reservoir rocks [3, 7]. A second group of research disciplines is dealing with transport of electrical and ionic charges by either diffusion or conduction through a solid phase in composite or porous materials. This type of transport is of importance for modern energy conversion technologies, which attempt to harvest green energy sources (e.g. transport of charged species in electrodes of fuel cells, solar cells or batteries) [8–12]. Thereby, it is necessary to understand which microstructural features influence the charge-transport, to improve the electrode performance by a controlled optimization of the microstructure. From the few mentioned examples, it becomes obvious that the question of how transport properties can be related to the microstructure is of high importance in many different fields.

In the discussion of the microstructure effects, porosity (ε), tortuosity (τ) and constrictivity (δ) are usually considered as the most important parameters. The topological description of τ and δ requires 3D information. Fortunately, the methods for 3D-microstructure characterization by means of micro- and nanotomography have significantly improved over the last couple of years, see, e.g. studies based on synchrotron X-ray tomography [13], FIB-tomography [14, 15], electron tomography by TEM [16], or 3D analysis with confocal laser scanning microscopy (CLSM) [17]. Since modern imaging techniques can provide reliable 3D-data down to the nanometre scale for nearly all material types, major problems are now related to the processing of the 3D images and to the geometrical definition of the associated microstructure parameters. It is important to note that a couple of years ago 3D information was much more difficult to obtain, and hence the classical theories of microstructure effects are usually based on the exploration of simplified geometries such as pore structures with cylindrical tubes or granular textures of mono-sized spheres. It is relatively easy to determine microstructure parameters for these simplified geometries. However, in most practical applications the materials have disordered microstructures and the quantitative description of transport relevant features for these structures is still a challenging task. Suitable geometrical definitions and suitable algorithms for the corresponding 3D image analysis are largely missing. Nevertheless, considerable progress in the field of 3D image analysis was achieved in recent years. For example, skeletonization techniques and graph theory are now widely used to measure the geometric tortuosity (τ_{geo}) directly from tomographic 3D-reconstructions of the complex microstructures [18, 19]. Of particular importance for this study is the concept of a so-called continuous-pore size distribution (c-PSD, introduced by Münch and Holzer [20]) and computational tools which allow the simulation of mercury intrusion porosimetry (MIP). As will be discussed in this article, the c-PSD and MIP-simulation

techniques open new possibilities for a quantitative description of bottleneck effects (i.e. constrictivity) in complex microstructures.

In the subsequent sections, the relevant literature, which deals with microstructure effects on the macroscopic transport properties, is briefly discussed. Thereby, we are focusing on a traditional approach, where the microstructure is described by volume averaged parameters for porosity (ε), tortuosity (τ) and constrictivity (δ). Fluid dynamics and transport simulations by finite element and lattice Boltzmann techniques are not considered here because these simulations usually do not provide a quantitative description of the microstructure but rather they provide the effective transport properties directly. A further simplification in our discussion considers the treatment of different transport mechanisms. In a generalized treatment of the microstructure effects, many different mechanisms should be taken into account (e.g. conduction, diffusion, flow). However, in this study we will mainly focus on conductivity (σ) and consider it as a process, which to a first approximation is influenced by the same microstructure parameters as most other transport mechanisms (e.g. diffusivity, D). Hence, for simplicity, in the equations of the following sections the terms σ and D are exchangeable.

The microstructure effects are described here with respect to their influence on the so-called relative conductivity (σ_r), which is defined by the ratio of the effective conductivity in a structured media over the intrinsic conductivity in a non-structured media (σ_{eff}/σ_0). A frequently used empirical law, which describes the impact of the pore structure on σ_r is based on the studies of Archie [3], who presented experimental data from sedimentary borehole samples. Thereby the so-called formation factor (F) was defined as the inverse of the relative conductivity ($1/\sigma_r$). A linear trend is obtained when log F is plotted versus log ε (porosity) for a series of samples with different porosities. The slope (m) in this logarithmic plot can then be used to define a power law relationship between porosity (ε) and the relative conductivity (σ_r), which is called Archie's law [3]:

$$\sigma_r = \frac{\sigma_{eff}}{\sigma_0} = \frac{1}{F} = \varepsilon^m. \quad (1)$$

It is important to note that Archie's law represents a purely empirical description and it does not help to identify the morphological features of the microstructure, which are actually dominating the transport properties. Hence, the power law relationship between porosity (ε^m) and relative conductivity (σ_r) only holds for a series of samples from the same geological formation, because these rocks have similar microstructures (i.e. similar grain shapes, similar dimensions of bottlenecks). Therefore, each type of microstructure (e.g. in different geological formations) will reveal a different exponential factor (m). Hence, the m-factor does not discriminate between the different morphological features, which could influence the transport properties.

As a step further, tortuosity (τ) is then often considered as an important feature of the microstructure, which may dominate the transport properties. The concept of tortuosity, which describes the effects of convoluted transport pathways and variations of the pore path lengths, was introduced by Kozeny [1] and then further refined by Carman [2]. The tortuosity concept was successfully applied to many different transport problems. This, however, also led to many different definitions for the tortuosity (i.e. geometrical, hydraulic, electrical, dielectrical and diffusional tortuosities). It is beyond the scope of this article to discuss these different tortuosities in detail. An excellent review and a 'guide through the maze' is given by Clennell [21]. Here, we briefly discuss some basic aspects and obvious problems of the tortuosity concept: In earth science and in chemical engineering [22], the tortuosity-effect is described by the following equation, where $0 \leq \varepsilon \leq 1$ and $\tau \geq 1$:

$$\frac{\sigma_{eff}}{\sigma_0} = \frac{\varepsilon}{\tau}. \quad (2)$$

A major problem in this context is the fact that there were no methods available until recently which enabled to measure tortuosity directly from the microstructure. Therefore, τ was usually indirectly determined, by substituting the measured σ_0, σ_{eff} and ε into Eq. 2 and then resolving for τ. We call this indirectly measured parameter the experimental tortuosity (τ_{exp}), which must be strictly distinguished from the geometrical tortuosity (τ_{geo}). New image analysis techniques nowadays enable the measurement of τ_{geo} directly from tomographs [18, 19]. Significant differences are usually then perceived between τ_{geo} and τ_{exp}, which indicates conceptual differences between the two types of tortuosity. The advantage of τ_{geo}, in contrast to τ_{exp}, is the fact that it is geometrically defined (e.g. pore path lengths along the central axis are commonly measured). Nevertheless, some uncertainties for τ_{geo} have to be mentioned. A first uncertainty can be related to the applied skeletonization algorithm and to the definition of the pore pathways. The chosen skeletonization algorithm will influence the extracted topology of the 3D graph. In addition, the selection of pathways through a complex connected pore network can be based on different criteria. Often the shortest path tortuosity is calculated [23]. Alternatively, the selection of the pore pathways can also be based on other criteria than shortest lengths (e.g. high permeability paths for maximal flow, see, e.g. [24]). Hence, a proper use of τ_{geo} should always be based on a clear definition of the underlying algorithms to describe a reproducible methodology.

Whereas a proper definition of τ_{geo} is in principle straight forward, the geometrical aspects of τ_{exp} are always ill-defined because of the indirect determination method.

This ill-defined state opened ample space for many hypotheses and for intuitive thinking about the geometrical features and the processes, which might be included in the experimentally determined tortuosity. According to many of these intuitive definitions, experimental tortuosity is not a pure microstructure parameter, because it depends also on the transport regime and on the associated experimental parameters. For example the so-called hydraulic tortuosity describes the lengths of the streamlines. Those streamlines, however, are dependent on 'external parameters' such as the applied pressure gradient and the viscosity, which is itself a function of temperature and chemical composition. Hence, the hydraulic tortuosity (as a representative for various types of τ_{exp}) is not a pure microstructure parameter, because it is not strictly describing the internal morphology. For the concept of this article, where we try to establish a quantitative relationship between the sample's microstructure (i.e. its internal morphology) and the corresponding effective transport properties, the geometrically well-defined τ_{geo} is considered to be of higher relevance than the ill-defined τ_{exp}.

In the context of a short literature review, it must be mentioned that many experimental studies were performed to formulate a quantitative relationship between τ_{exp}, ε and the corresponding transport properties. Thereby an almost innumerable amount of empirical expressions was derived (see reviews by Boudreau [25] and Shen and Chen [26]). The fact that no unifying expression could be found indicates that τ_{exp} is maybe not a reliable parameter for the description of the microstructure–property relationship. An additional and severe problem with τ_{exp} is the very high values (up to 20), which can be obtained with the indirect measurement of tortuosity [7, 22, 27, 28]. Geometrical models for the pathways in granular media show that such high tortuosities are clearly not realistic [22]. In order to obtain more realistic values for tortuosity, τ^2 was introduced in Eq. 2 instead of τ, see discussions in Carman [2], Kozeny [1] and Clennell [21]. In this context, it is important to note that some authors calculate tortuosity from effective path lengths $(l_{eff})^2$ with exponent of 2. Hence, different definitions of tortuosity are found in the literature (e.g. $\tau_{Carman} = (l_{eff}/l_0)^2$, and $\tau_{Kozeny} = l_{eff}/l_0$), which leads to considerable confusion. In any case, the exponent of 2 is not rigorously derived, but it was motivated mainly by the intention to fit the exponential data with reasonable values for tortuosity (τ_{exp}).

An alternative explanation for the unrealistically high values of τ_{exp} is the hypothesis that additional geometrical features, which influence transport properties, are captured erroneously by the indirect determination method. These additional geometrical features should be described explicitly in refined transport models. In this context, constrictivity (δ) was introduced as an additional parameter, which influences the transport properties [29]

$$\frac{\sigma_{eff}}{\sigma_0} = \frac{\varepsilon\delta}{\tau}. \tag{3}$$

Constrictivity (δ) is a dimensionless parameter with values between 0 (e.g. for trapped pores) and 1 (e.g. for cylindrical pores with constant radius). It contributes to a transport resistance, which is inverse proportional to the width of the bottlenecks. In a similar way, as mentioned for the tortuosity, there was also no method available in the past, which enabled the determination of constrictivity directly from disordered microstructures. Furthermore, a geometrical definition of δ is still lacking. Therefore, it must be assumed that in most experimental studies the constrictivity effect is tacitly included in (unrealistically high) τ_{exp} due to the lack of suitable measurement techniques.

Nevertheless, mathematical expressions for the bottleneck effect were developed a long time ago, but only for ideal, simplified geometries. Petersen [30] introduced a mathematical expression, which describes the effect of constrictions on the diffusion through a single cylindrical pore. In his model, the pore has hyperbolic necks so that the cross section varies periodically along its length. In his description, Petersen [30] used a constriction factor ($\beta_{Petersen}$), which was defined as follows:

$$\beta_{Petersen} = \frac{A_{max}}{A_{min}}, \tag{4}$$

where A_{min} is the pipe cross section at the constriction and A_{max} is the cross section at the pore entrance and/or at non-constricted 'bulges' in the pipe. By solving the diffusion equations for this geometry, Petersen showed how the effective diffusivity depends on the variation of the cross section. By analysing the graph from Petersen [30] one obtains the following analytical relationship:

$$\frac{D_{eff}}{D_0} = 0.2122\ln(\beta_{Petersen}). \tag{5}$$

Michaels [31] developed a similar relation as Petersen [30], but which also takes into account the distance between bulges and constrictions. From his analysis, it follows that the variation in cross-sectional area (i.e. β) has a much higher impact on the effective diffusivity than the distance between bulges and constrictions. Hence, for the characterization of the bottleneck effect in real microstructures, it is mainly necessary to find a suitable methodology, which enables to quantify the cross-sectional area at the constrictions and at the bulges.

Petersen implicitly distinguished between the constriction factor ($\beta_{Petersen}$) and the constrictivity (δ). $\beta_{Petersen}$ is geometrically well-defined, but limited to a simplified geometry of a single tube. In contrast, δ is used in

macroscopic models to describe bottleneck effects (e.g. Eq. 3). However, at that time δ could not be measured experimentally and it was, therefore, not defined geometrically. For the distinction between β and δ it is important to note that Petersen's description of β considers a 'superficial' case, where porosity and tortuosity are equal to 1 (i.e. consideration of a single pipe). For this case, the constriction factor directly relates to the relative diffusivity (see Eq. 5) and β is identical with τ. However, for the 'interstitial case' of porous media with complex microstructures, no mathematical description of the constriction effect is yet provided. Hence, at this stage, the relationship between constriction factor (β, as defined in Eq. 4) and constrictivity (δ, as applied in Eq. 3) is not yet established. Petersen made the following conclusion: 'Although the concept of pore constrictions provides the basis for a reasonably attractive explanation of abnormally high tortuosity factors, unfortunately there appears to be at present no satisfactory experimental technique to characterize independently the structure of pores in sufficient detail to test the (constrictivity) method.'

The present investigation focuses on the elaboration of new methodologies, which enable the quantitative description of bottlenecks directly from tomographs of disordered microstructures. For simplicity in our study, we are using the inverse of Petersen's constriction factor (i.e. $\beta = 1/\beta_{\text{Petersen}}$), which then results in β values between 0 and 1, (similar to the constrictivity δ)

$$\beta = \frac{A_{\min}}{A_{\max}} = \frac{\pi r_{\min}^2}{\pi r_{\max}^2} = \left(\frac{r_{\min}}{r_{\max}}\right)^2 \tag{6}$$

As mentioned above, the proper geometrical definition and the reliable measurement of parameters in complex microstructures are challenging. In disordered microstructures, there is no uniform value for $r_{\min}$ and $r_{\max}$. The variation of these parameters has to be described by size distribution functions. Thereby, the methodologies introduced by Münch and Holzer [20] for continuous-phase size distribution (c-PSD) and for the simulation of MIP open new possibilities. MIP and c-PSD deliver two different results for the phase size distribution (PSD) of the same sample (Note: 'phase' can be particles/solid or pores). Whereas the MIP-PSD is dominated by the constriction effect, the c-PSD is explicitly insensitive to the effect of bottlenecks. Hence, c-PSD and MIP-PSD are considered as potential methodologies, which can be used to describe $r_{\max}$ and $r_{\min}$. The first part of this article focuses on fundamental geometrical aspects of the PSD-measurements to test the suitability and reliability of the proposed methods. If these tests are positive, then these methods enable the quantitative characterization of the constriction factor (β) directly from tomography. In the second part, we then use experimental data to establish an empirical relationship between β and δ, which is the basis for predictions of the macroscopic transport properties. Hence, the basic hypotheses of the present investigation are the following:

(I) The simulation of MIP can be used to describe the characteristic dimensions of the bottlenecks (constrictions), which results in a statistically averaged value for $r_{\min}$.
(II) In a complementary way, the concept for continuous-phase size distributions (c-PSD) can be used to characterize the typical dimensions of non-constricted bulges (i.e. $r_{\max}$).
(III) By combining MIP and c-PSD, the constriction factor (β) can then be extracted directly from tomographs of complex microstructures.
(IV) Based on experimental data (conductivity measurements) for σ_{eff} and microscopy data for τ_{geo} and ε, the constrictivity (δ) can be calculated indirectly from Eq. 3. In this way, the relationship between β (geometrical) and δ (experimental) can be described empirically.
(V) The effective transport properties on a macroscopic scale can then be calculated. These calculations are entirely based on the volume-averaged parameters from tomography (ε, $r_{\min}$, $r_{\max}$, β, τ_{geo}) and on the empirical relationship between β and δ.

Regarding the concept of this study it must be emphasized that transport in disordered microstructures includes a complex mechanism with numerous serial and parallel steps occurring at the same time. Therefore, it is a justified question whether the transport properties of complex networks can be calculated only on the basis of a few averaged morphological parameters. Consequently, it must be emphasized that the proposed parametric approach represents a heuristic solution and its validity has yet to be tested.

Materials and experiments

In this study, two material systems are investigated. First, a porous cathode for solid oxide fuel cells (SOFC) is used to test the measurement techniques (c-PSD and MIP), which are proposed for the determination of the constriction factor. More explicitly, the influence of geometrical features (i.e. variable sample thickness, local heterogeneities, small cracks and different intrusion directions) on the c-PSD and MIP-results is investigated, which is considered as a reliability test for the applied methodology. It should lead to a better understanding of which circumstances lead to a reliable constriction factor (β) and when the method fails. The second material system consists of porous diaphragms for alkaline electrolysis cells. These samples are investigated by a combination of impedance spectroscopy and X-ray tomography. The results are used to make a link between the

'microscopic' constriction factor (β) and the 'macroscopic' constrictivity (δ). The experimental techniques for the fabrication and investigations of the two materials systems are described subsequently in two separate sections.

FIB-tomography of porous SOFC cathodes

Cathode fabrication

The electrochemical activity of SOFC cathodes with different microstructures was investigated in a previous study by Prestat et al. [32], in which the fabrication and the experimental procedure is described in great detail. Powders of $La_{0.6}Sr_{0.4}CoO_{3-\Delta}$ (subsequently called LSC) were produced by flame spray synthesis [33]. The resulting powder had a bimodal particle size distribution, consisting mainly of nanopowder (15–20 nm) and an additional minor component of micropowder (>l μm). The averaged specific surface area of the as-prepared powder was 29 $m^2\ g^{-1}$ (BET). For screen-printing, pastes with a solid loading of 25 wt% (including LSC and pore-former) were prepared. Solsperse3000 (from Avecia) was used as a dispersant and Terpineol (from FLUKA) as the solvent. The LSC cathodes tend to form cracks during the sintering due to a strong shrinkage, which is caused by the high sinter activity of nanoparticles. In order to reduce the crack formation, graphite pore-former (Timrex KS4, $d_{50} = 2$ μm) was included in the paste mixture. The sample used in this study contains 23 wt% of LSC and 2 wt% of graphite. The pastes were screen printed on a $Ce_{0.8}Gd_{0.2}O_{1.9}$ electrolyte substrate, using a 75-μm mesh with a thickness of 36 μm. Sintering in air was performed at 850 °C (Sample name: LSC2/G2N23_850_H).

Microstructure analysis based on FIB-tomography

Focused ion beam (FIB) tomography of the sample LSC2 was performed according to the procedures described earlier [14, 15, 34–36]. The sample preparation included polymer impregnation, grinding and polishing. For impregnation of the pores, a polymer system with AralditBY158/Aradur21 (supplied by Huntsman) was used. Mechanical polishing was performed on textile substrates with diamond suspensions of 6, 3 and 1 μm (MetaDi mono-crystalline diamond suspension, Buehler). For the FIB-tomography experiments, we used a ZEISS NVision 40, which is located at the Electron Microscopy Centre at ETH Zürich (EMEZ). The FIB-procedure included the following steps: (a) gas-assisted metal deposition of a 1-μm thick Pt layer. The layer was applied only at the location of interest (20 × 20 μm) to protect the surface from ion milling artefacts. (b) Preparation of a cube with dimensions of 15 × 15 × 15 μm. A freestanding cube was prepared to reduce shadowing effects and re-deposition during the stack acquisition. (c) *Serial sectioning* automated acquisition of an image stack was obtained by repeated and alternating execution of erosion (FIB) and imaging (SEM).

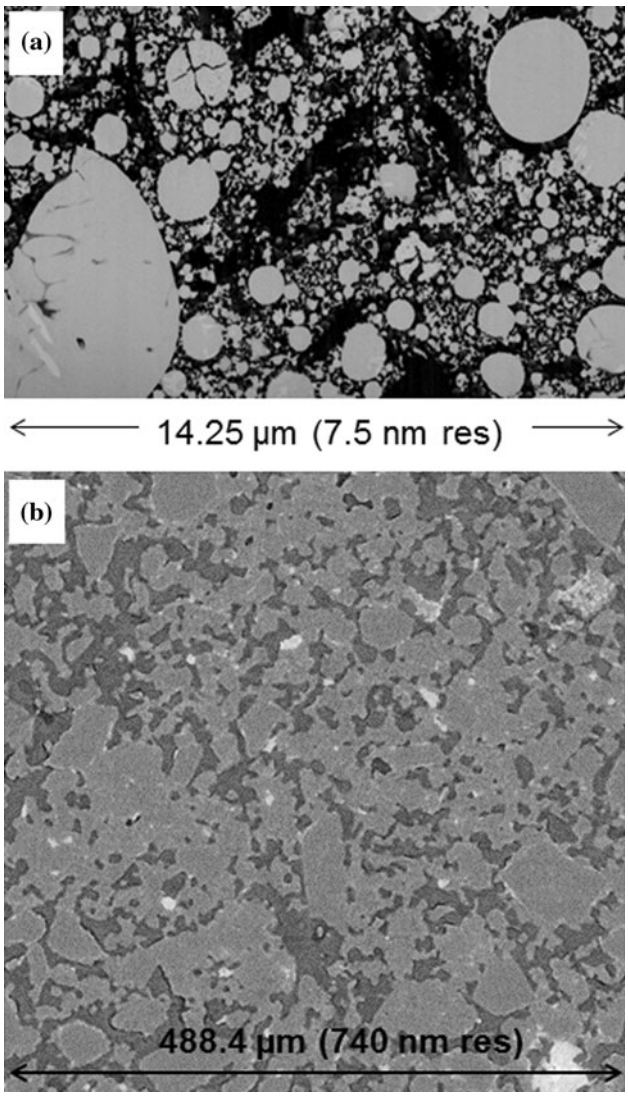

Fig. 1 Examples of raw data (virtual 2D slices) **a** from FIB-tomography of LSC cathode (pixel resolution 7.5 nm) and **b** from SRμCT of olivine membrane with 32 % porosity (voxel resolution 740 nm, after binning)

During serial sectioning the FIB-slicing was performed with an acceleration voltage of 30 kV and a beam current of 1.5 nA. The ESB detector was used for BSE imaging at low kV (i.e. 1.2 kV, aperture size 60 μm). The original image parameters were 2048 × 1536 pixels with a pixel size of 7.5 nm. Figure 1a illustrates the image quality in the raw data (i.e. 2D image). Excellent contrast is perceived between pore and LSC-phase. 1300 images were acquired with a slicing distance of 15 nm. The resolution in the raw data was then decreased to 1024 × 768 pixels with

a pixel size of 15 nm. Hence, the voxel size after binning of the raw data was 15 × 15 × 15 nm. In this context, it is important to note that the scan resolution (and its variation due to binning) may have a considerable influence on the quantitative results from image analysis. This is of particular importance when the feature sizes are in the same range as the pixel/voxel size. As shown in Fig. 4, the average particle sizes in the cathode-sample are more than 10 times larger than the voxel resolution after binning (i.e. r_{50} c-PSD = 157 nm). Even the dimensions of the narrow bottlenecks are 4–5 times larger than the voxel size (i.e. r_{50} MIP-PSD = 66 nm). A small portion of the features (few vol.% of the particles and pores) has sizes in the range of the voxel. Those few vol.% are the features, which cannot be captured precisely and reliably.

The procedure for the subsequent image analysis consisted of (a) alignment of the stack, (b) cropping of a region of interest (cube size 14.4 µm × 9.4 µm × 7.6 µm), (c) noise filtering, (d) segmentation, (e) visualization and (f) quantification. For the steps (a)–(e), the software packages Fiji (http://fiji.sc/wiki/index.php/Fiji) and Avizo (http://www.vsg3d.com/avizo/overview) were used. For the quantitative analyses (f) with c-PSD and MIP-PSD, we used homemade software, which was developed with Matlab and Java. The corresponding algorithms were presented and discussed in a separate publication by Münch and Holzer [20]. The simulation of MIP and the concept of continuous size distributions (c-PSD) are re-examined in this article (see sections 'Methodology for quantification of the constriction factor (β)' and 'Geometrical tests'), under the view of their potential suitability for the quantitative description of bottleneck effects in complex microstructures.

The most time-consuming processing step with respect to computation is the MIP-simulation. Thereby, the computing time depends on the features sizes (computation of 3D distance maps) and on the size of the data volume. With the present cathode-sample (ca. 1000^3 voxels), each MIP-simulation takes about 30 min (on a Linux machine with multi-core processors and with 96 GB RAM). It is, however, important to note that the most time-consuming part of the data processing are not the individual computation steps, but it is rather the preparation of some delicate calculations (i.e. decision which parameters to choose, e.g. for segmentation). Some of these steps cannot be done automatically and they require careful (manual) evaluation, e.g. by try and error with down-sampled data cubes.

Porous diaphragms for alkaline electrolysis cells

The influences of pore structures on effective ion conductivities of olivine- and wollastonite diaphragms were investigated in a separate study by Wiedenmann et al. [37]. The focus in the previous study was mainly on the investigation of the porosity (ε), effective porosity (ε_{eff}) and geometric tortuosity (τ_{geo}) parameters. The results of this previous study show that the measured geometric tortuosity cannot account for the variations of the macroscopic ion conductivity. In this study, we are re-examining this set of data from porous diaphragms, with a special focus on the constriction effect. In the previous paper [37], the impedance spectroscopy and the fabrication procedures are described in greater detail, but a short summary is presented here.

Sample fabrication and electrical impedance spectroscopy (EIS)

Two series of porous diaphragms consisting of olivine and wollastonite were prepared by sintering of uniaxially pressed green bodies (20 MPa) at 1300 °C. The porosity was changed systematically by adding different amounts of carbon pore-former (Sigradur carbon powder). The final porosity (ε) varies from 0.27 to 0.44 for olivine, and from 0.45 to 0.80 for wollastonite.

EIS was performed with a four-electrode electrochemical cell, by applying a frequency range from 0.1 to 100 kHz using a Zahner IM6eX potentiostat. The applied potential between the sense and reference electrodes was 0.75 V, to which an AC signal with amplitude of 10 mV was added. The pores of the diaphragm were saturated with an electrolyte solution (25 wt% potassium hydroxide), which has an ionic conductivity (σ_0) of 0.645 S/cm. As the porous diaphragm consists of isolating material, no imaginary part is recorded with EIS and hence a purely ohmic resistance is measured, from which the effective ionic conductivity (σ_{eff}) of the porous diaphragms can be determined.

Microstructure analysis based on X-ray absorption tomography

Synchrotron radiation microcomputed tomography (SRµCT) was performed at the Swiss Light Source (SLS, Tomcat beam line) at the Paul Scherrer Institute (PSI) in Villigen, Switzerland. For each sample, the Tomcat experiments provided stacks of 2048 images with a matrix of 2048 × 2048 pixels and a pixel resolution of 370 nm. The experiments were performed with X-ray energy of 15.5 keV and a field of view of 0.78 mm. From the raw data volume, sub-cubes were cropped at the region of interest with a matrix of 660 × 660 × 660 voxels, and a voxel size of 740 nm. A virtual 2D-slice from the raw data (after binning) is shown in Fig. 1b for olivine with 32 % porosity. Most features (i.e. olivine particles and pores) have a size, which is much larger than the binned voxels,

which is a precondition for reliable determination of microstructure parameters. The subsequent quantitative characterization of the pore structure by means of 3D image analysis includes the following steps: (a) filtering, segmentation and determination of porosity (ε), (b) skeletonization and graph analysis for the measurement of geometric tortuosity (τ_{geo}) and (c) MIP- and c-PSD analyses for determination of the constriction factor (β).

Filtering and segmentation was performed with the software packages from Fiji and Avizo. For the characterization of the geometric tortuosity, the segmented pore network is first transformed into a voxel-skeleton using the tools provided by Avizo [38]. The Avizo software uses an approach, which detects ridges in distance maps by applying a thinning algorithm, which results in a string of connected voxels in the centre of the pores. The distance to the nearest boundary is stored for every centre voxel. The skeleton is then transformed into a 3D graph [39]. For the determination of the geometric tortuosity, the shortest pathways between the inlet and the outlet faces of the data cube are analysed with a homemade Matlab-code. Thereby, the shortest pathways through the pore network are identified with the running Dijkstra's algorithm [40]. For each shortest pathway, the geometric tortuosity is then statistically described by measuring the length of the convoluted line and the length of the corresponding vector between inlet and outlet. The geometric tortuosity is defined by the ratio of the two measured lengths. More details about the geometric tortuosity measurements are given in Keller et al. [19, 41]. The MIP- and c-PSD analyses are performed according to the methodology presented in Münch and Holzer [20], to measure r_{min}, r_{max} and β. These two methodologies are discussed in the following sections.

Results and discussion

Methodology for quantification of the constriction factor (β)

For the investigation of the constriction effects new methods are required which enable a quantitative description of the bottleneck dimensions (r_{min}) and of the bulges (r_{max}) directly from complex, disordered microstructures. Conventional image analysis methods usually intend to measure the size of single, isolated objects (pores or particles). Thereby, the definition of discrete objects from a percolating network represents a major difficulty. In order to circumvent the problems related to object recognition, we have developed an alternative concept of a so-called continuous-phase size distribution (c-PSD) [20]. It was shown that the c-PSD method enables a reproducible, statistical characterization of complex phase networks [36]. In addition, also a method for the simulation of MIP was presented [20]. Both methods are based on the same geometrical concept: The volume fractions, which can be filled with spheres of given radii are measured. In a physical sense, the curvature of the spheres relates to a surface tension (e.g. of the intruding mercury). In comparison with the c-PSD method, the MIP-measurement includes an additional simulation step, which is the intrusion in a predefined spatial direction. This additional step is the reason for very different perceptions of the size distributions. Thereby, the c-PSD method mainly captures the size of the bulges and of the non-constricted domains (r_{max}), whereas the MIP-PSD method characterizes the dimensions of the necks between the bulges (r_{min}).

Continuous-phase size distribution (c-PSD)

In this section, we only summarize the basic principle of the c-PSD method from Münch and Holzer [20]. First of all, it is worth mentioning that the c-PSD method can be applied to both, the pore and the solid phases. As illustrated in Fig. 2, the segmented phase (a) is first transformed into a distance map (b), whereby the colour code represents the shortest distance to the phase boundary (dark blue = 0 nm, red = 435 nm). The volume fraction is measured which can be occupied by a sphere of a specific radius without crossing the phase boundary. The sphere radius can be considered as the curvature of a meniscus from an intruding liquid (e.g. mercury). By decreasing the radius, a larger volume can be occupied, which is shown in Fig. 2 for four incremental steps with radii of 435 nm (c), 400 nm (d), 250 nm (e) and 100 nm (f). By plotting the radii versus the corresponding filled volumes, a cumulative c-PSD curve is obtained (Fig. 2g). The domains at the constrictions have little influence on the c-PSD-measurements because these domains contribute only a relatively small volume fraction. Hence, the c-PSD-curves predominantly reflect the dimensions of the voluminous bulges.

In Fig. 2, the distance map has only one local maximum where the largest sphere can be placed. In a complex microstructure, the distance map has numerous local maxima where the processes of decreasing sphere radii can be initiated. This is shown in Fig. 3a, where the c-PSD method is applied for size measurements of LSC-particles in the porous SOFC cathode (sample LSC2). The colours in Fig. 3a reflect the c-PSD radii whereby the largest particles in red have 'c-PSD radii' up to 1200 nm. A large portion of the LSC-phase, which is shown in bright blue to green, consists of smaller particles with radii in the range of 100–500 nm. As shown in Fig. 4, the c-PSD curve exhibits a wide distribution of particle sizes between <100 and 1200 nm, which is compatible with the qualitative observations in Fig. 3a.

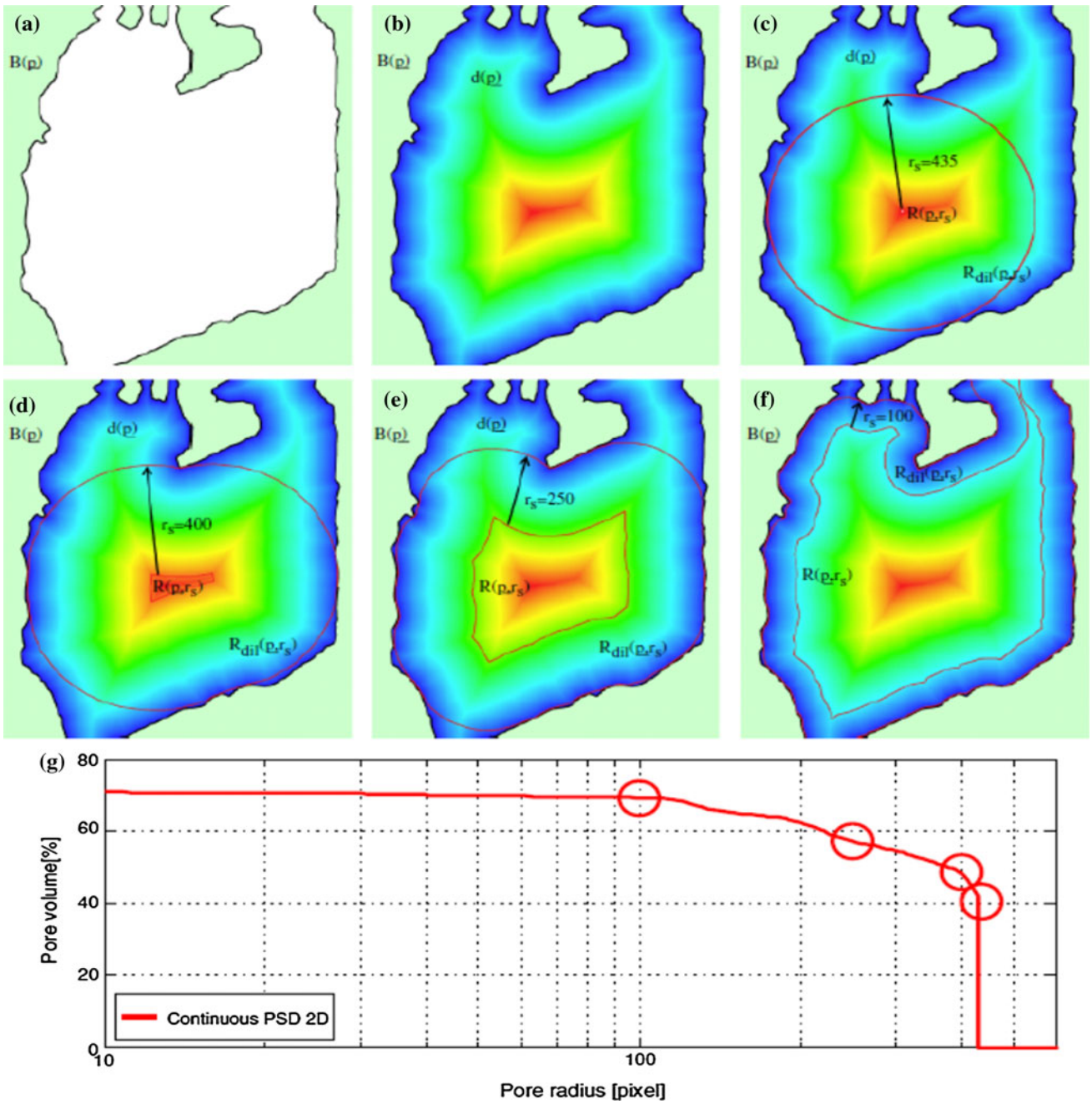

Fig. 2 Illustration of the continuous-pore size distribution (c-PSD) method, from Münch and Holzer [20] (reproduced with kind permission from JACerS). The pore object (**a**), which is transformed into a coloured distance map (**b**) is filled with a sphere of maximum radius (**c**) whose centre is placed at the local maximum of the distance map. The sphere radius is then decreased continuously and the smaller spheres can 'intrude' smaller pores and constrictions. Hence, more pore space is filled when decreasing the radius (**c**–**f**). This leads to a continuous size distribution curve (**g**, c-PSD-curve) where the filled pore volume relates to the corresponding spherical radius (Color figure online)

Simulation of MIP

MIP is a well-known physical testing method, which is widely applied in materials, earth and environmental sciences for the characterization of porous media. The MIP-PSD is obtained by filling the pore space with liquid mercury while increasing the capillary pressure. For each step with incremental pressure increase, the corresponding volume of the intruding mercury is recorded, which reveals the experimental MIP-PSD. An inverse relationship between capillary radius (R_c) and capillary pressure (P_c) is defined by the (simplified) Washburn equation [42, 43], where γ represents the surface tension and φ is the wetting angle

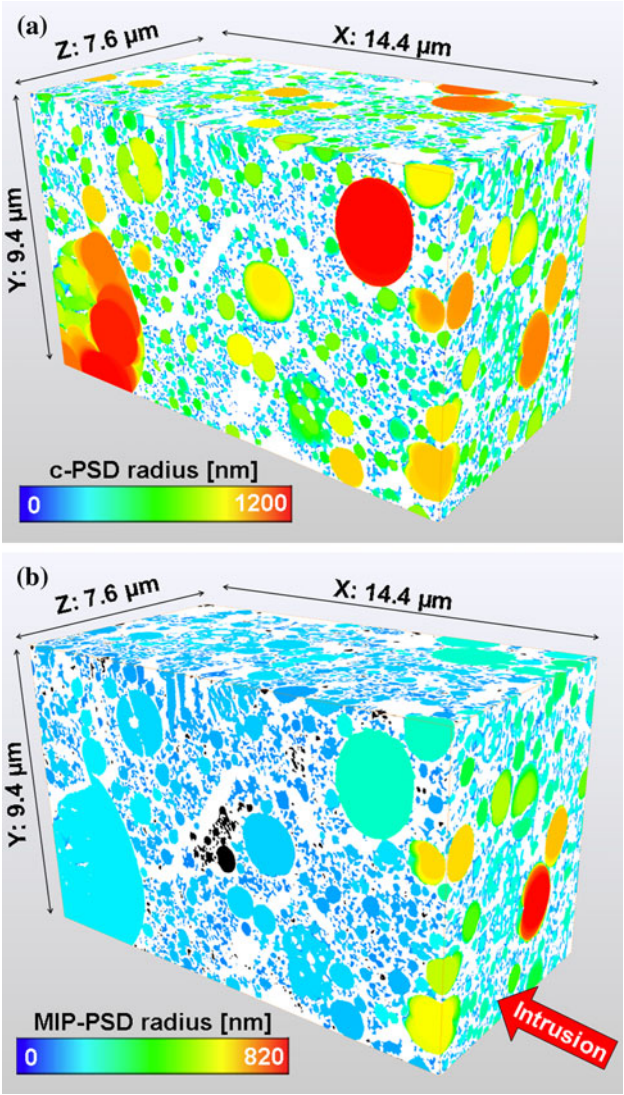

Fig. 3 Image volume from FIB-tomography (voxel resolution: 15 nm), which represents the microstructure of a porous SOFC cathode with particles of $(La,Sr)CoO_3$ (sample name: LSC 2). **a** The *colour code* represents the particle radii resulting from the c-PSD analysis. **b** Illustration of the MIP-simulation. The intrusion starts at the *y*–*z*-plane on the right side of the cube and it propagates along the *x*-axis to the left through the LSC-phase. The *colour code* represents MIP radii between 820 nm (*red*) and 1 nm (*dark blue*). Disconnected particles are *black*. Pore space is *white* (Color figure online)

$$P_c = \frac{2\gamma}{R_c}\cos\varphi. \tag{7}$$

Mercury intrusion can be simulated based on tomography data by applying the same geometrical concept as used for c-PSD [20], but with a modification of the algorithm which introduces a specific 'growth criteria' for the intrusion process. Thereby, the intrusion is simulated by continuously decreasing the curvature radii of the menisci (equivalent with an increase of P_c). During the mercury intrusion simulation, the capillary radius can never

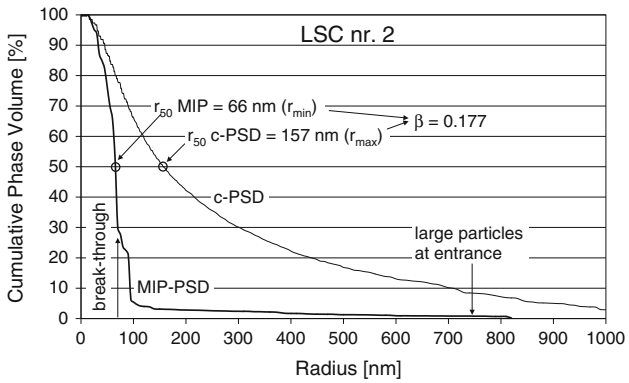

Fig. 4 Comparison of particle size distributions (c-PSD and MIP-PSD) for the LSC perovskite phase in a porous SOFC cathode. The PSD-measurements are based on the same image volume from FIB-tomography (see Fig. 3a, b). Note the significantly smaller radii ($r_{50} = 66$ nm) of the MIP curve compared to the c-PSD curve ($r_{50} = 157$ nm). This difference is attributed to the bottlenecks which strongly influence the MIP-PSD, but which are hardly affecting the c-PSD-measurements

increase. This corresponds to the fact that in the physical MIP experiments the pressure is continuously increased. Hence after passing a bottleneck, the volume of the following bulge is attributed to the radius (or pressure), which is necessary to pass the smallest constriction (neck) along the preceding pore pathway. This is called the bottleneck effect and it leads to MIP-PSD-curves, which clearly overestimate the volume of small pores. In MIP measurements, a so-called breakthrough is frequently observed, which occurs when the curvature radius is reduced to a certain threshold value that corresponds to the characteristic dimension of the transport limiting constrictions. Beyond this radius, a major portion of the pore volume is accessible for the intruding liquid. Hence, in contrast to the c-PSD, the MIP-PSD predominantly captures the size of the bottlenecks (i.e. a large volume is attributed to the breakthrough radius). For a thorough discussion of the bottleneck effect, see also Diamond [44].

The size distribution of a MIP-simulation is illustrated in Fig. 3b for the same SOFC cathode as shown in Fig. 3a for the c-PSD. The mercury intrusion, which is simulated through the network of the solid phase (not pores), is initiated on the right side of the cube (*y*–*z*-plane) and it propagates to the left (*x*-direction). The colours reflect the distribution of MIP radii. At the pore entrance on the right side, MIP captures the non-constricted radii at the bulges in the range between 450 nm (green) and 820 nm (red), similar to c-PSD. While propagating from right to left, the MIP radii are rapidly decreasing due to the constrictions, which typically have radii around 66 nm (blue). The blue colour thus represents the domains where the intrusion is dominated by the breakthrough radius. The distribution of the blue colour in Fig. 3b indicates that the typical break-through radius is already reached at short intrusion depths

of 2–5 μm, which corresponds to 2–5 times the radius of the largest particles.

Comparison of c-PSD and MIP-PSD

The MIP- and c-PSD-curves of the LSC cathode are shown in Fig. 4. In the MIP-PSD curve, more than 90 % of the LSC volume is smaller than 100 nm, which is attributed to the bottleneck effect. In the MIP-PSD, only 5 % of the LSC volume has radii larger than 200 nm. The MIP-PSD curve thus shows a striking discontinuity, which is interpreted as a result of the so-called breakthrough. Due to this strong discontinuity, the r_{50} from the MIP-PSD curve can be considered as a reliable measure for the dimensions of the necks between the LSC-particles (i.e. r_{min}). The variation of the MIP radii is only 15 nm when changing from the 30 to the 70 vol.% fractile (i.e. from $r_{30} = 70$ nm to $r_{70} = 55$ nm). In this example it is thus not very important which fractile is used for the definition of r_{min}. For simplicity, throughout this study we will define r_{min} as being equal to r_{50} from MIP-PSD.

In contrast to the discontinuous MIP-PSD, the c-PSD curve spreads over a wide range of particle sizes up to 1200 nm. This wide range of particle sizes corresponds well with the qualitative observations in Fig. 3a. The 50 vol.% fractile (r_{50}) of the c-PSD curve is 157 nm, which is 2.5 times larger than the r_{50} from MIP-PSD. The r_{50} from c-PSD is considered here as a measure for the mean particle size (i.e. r_{max} as a statistical measure for the 'non-constricted bulges'). Using r_{min} and r_{max} according to Eq 6, the resulting constriction factor (β) is only 0.18. This low value for the constriction factor documents the morphological limitations for transport processes (e.g. electronic or ionic conductivity), which are caused by the narrow contacts between the LSC-particles.

Geometrical tests

Sample thickness, local heterogeneities and representative volume

FIB-tomography is based on a time-consuming serial sectioning procedure. Consequently the 3D-data cubes from FIB-tomography are often limited in thickness. This limitation raises the question of which size of 3D-image window is required for a representative analysis. For the MIP-simulation this question is linked with the break though phenomena. At the pore entrance, the MIP radii are not yet constricted and hence it can be expected that in this region they are identical or similar to the c-PSD radii. With increasing path lengths, the MIP radii decrease until they reach the so-called breakthrough radius. The question arises how long the intrusion paths have to be before the breakthrough radius is reached. We call this path length the critical intrusion depth (ID_{crit}). This question is empirically addressed here by repeatedly performing the MIP-simulation for a FIB-cube of the LSC cathode, whereby the thickness of the cube is gradually increased. The thickness of the data cube is increased in the z-direction in steps of 75 nm up to 1.5 μm, and then in steps of 1.25 μm up to 7.6 μm. The results are illustrated in Figs. 5, 6 and 7.

Figure 5 shows the MIP-simulation for the entire data volume from FIB-tomography (i.e. maximum thickness). The LSC-phase (Fig. 5a) shows a pronounced constriction effect. At the front face, large 'non-constricted' radii are recorded (shown in red, yellow and green). Due to the bottleneck effect, the MIP radii decrease rapidly to <100 nm (blue). The critical intrusion depth (ID_{crit}) is reached after approximately 3 μm. At longer intrusion depths the MIP radii are dominated by the constrictions, which typically have a breakthrough radius of 66 nm. The bottleneck effect leads to a uniform blue colour at intrusion depths larger than 3 μm (ID_{crit}). It should be noted that the size distribution of LSC is wide and that the volume of the FIB-cube is obviously too small for a statistical representation of the largest objects. For example, the large, red particle in the front left part of Fig. 5a appears to be a singularity in the probed sample volume. The question arises to what extent such large single particles will influence the resulting MIP-PSD (which is discussed below).

In contrast to the LSC-phase, the intrusion into the pore-phase (Figs. 5b, c) is less affected by constrictions. Therefore, the MIP radii do not change significantly with increasing intrusion depth (constant colour range: bright blue to green). However, it should be noticed that the pore structure includes a crack, which is located in the back left part of the cube (Fig. 5c). This crack is not visible at the front plane of the cube (Fig. 5b). In this case, also the question arises whether the crack will influence the resulting MIP-PSD and the associated r_{min}.

The PSD-curves resulting from repeated MIP-simulations and gradually increasing the cube thickness are shown in Fig. 6a (for LSC) and b (for pores). When the sample is very thin (75 nm), then the MIP radii of the LSC-phase (a) are not yet constricted and hence the size distribution is wide. With increasing sample thickness, the bottleneck effect becomes more pronounced, which leads to PSD-curves with a marked discontinuity. Below the critical intrusion depth (ID_{crit}), r_{50} decreases gradually when the thickness is increased. Above the ID_{crit} (thickness >3 μm), the r_{50} radii remain constant at 66 nm, which then give stable results for the r_{min}. It can be concluded that the inhomogeneous spatial distribution of single large particles (see Fig. 5a) does not affect the MIP-PSD when the sample thickness is larger than the ID_{crit}.

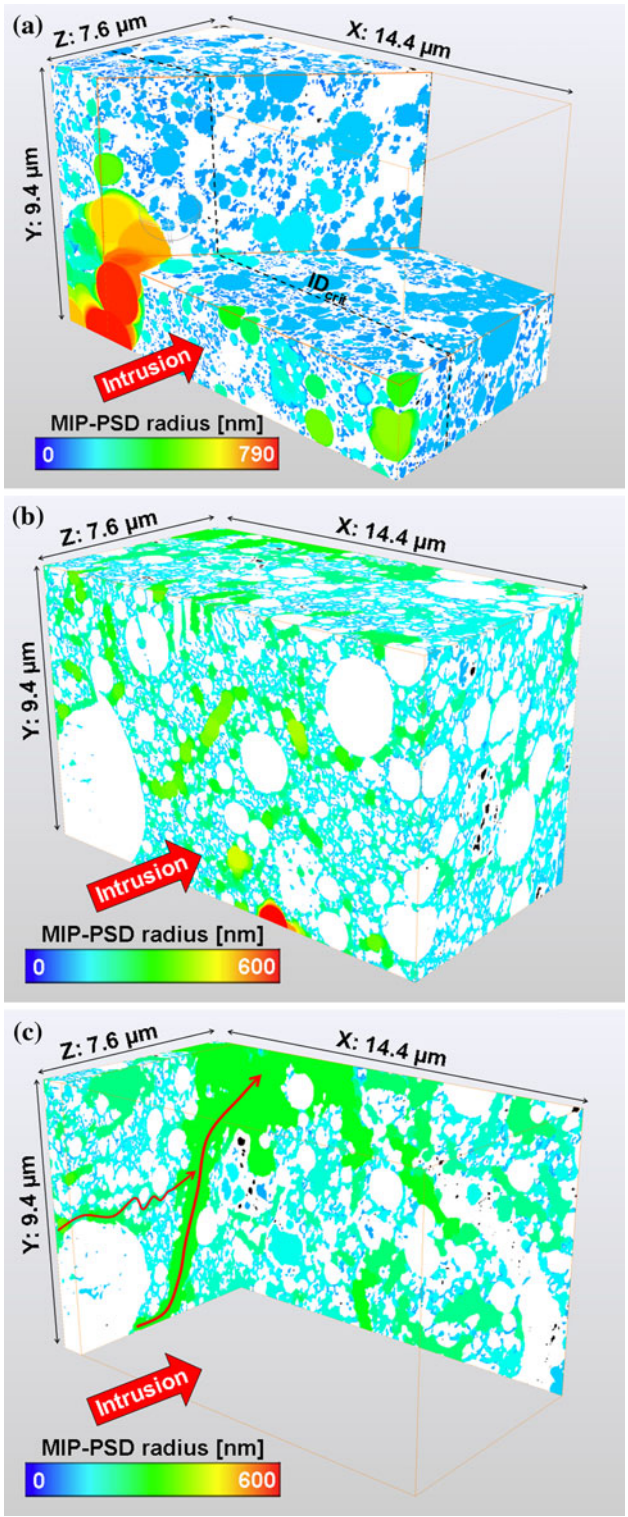

◀ **Fig. 5** Simulation of mercury intrusion for a porous LSC cathode (**a** intrusion of LSC-phase; **b**, **c** intrusion of pore-phase). The MIP intrusion of the LSC-phase (**a**) shows a pronounced constriction effect. The critical intrusion depth (ID_{crit}) is reached after approximately 3 µm. At the intrusion entrance (*x*–*y*-plane) the LSC-particles show a wide size distribution and the statistics for a representative analysis of the largest particles (*red*) is very poor. The MIP intrusion of the pore-phase (**b**, **c**) is less strongly affected by constrictions. Therefore, the MIP radii of the pores do not change significantly with increasing intrusions depth. However, the pore structure shows a crack in the *back left part* of the cube (**c**), which may trigger a breakthrough event (Color figure online)

In contrast to the LSC-phase, the bottleneck effect is rather weak in the pore-phase and hence, the MIP-PSDs do not change significantly with increasing sample thickness (Fig. 6b). The r_{50} values only decrease from 75 nm at the pore entrance to 64 nm at a thickness of 4.5 µm. A 'mini break through' then occurs at an intrusion depth of 5 µm. This partial breakthrough is attributed to the presence of a small crack in the back part of the FIB-cube (see Fig. 5b). Due to the crack and associated mini breakthrough, the r_{50} increases again to 84 nm. In this example, the MIP-PSD is not significantly affected by the short crack, because this crack does not cross the entire sample. The crack is only infiltrated via pore pathways, which have the characteristic bottleneck dimensions of the average pore structure.

In Fig. 7, the r_{min} and r_{max} from repeated MIP-PSD and c-PSD analyses are plotted versus the corresponding sample thicknesses. In the LSC-phase (a), the pronounced bottleneck effect leads to a rapid decrease of the r_{min} from initially 230 to <100 nm within the first 2 µm. At thicknesses larger than the critical intrusion depth (3 µm), the r_{min} reaches a constant plateau at 66 nm. Above the ID_{crit}, the observed structural heterogeneity (changing volume fraction of LSC) does not affect the stability and reproducibility of the r_{50} from MIP for LSC. In contrast, the r_{50} from the c-PSD measurement of LSC changes gradually. This instability is most probably caused by a single, exceptionally large LSC-particle in the front part of the FIB-cube (see Fig. 5a). Nevertheless, at larger thickness (>6 µm), the slope of the r_{max} from c-PSD becomes shallow and approaches a constant value around 150 nm. Consequently, the constriction factor is also changing with thickness but it approaches a plateau with $\beta = 1.77$ at thicknesses >6 µm. Hence, for the LSC-phase the MIP analyses and the corresponding r_{min} are hardly affected by local heterogeneities, because they are dominated by the strong constriction effect. The critical MIP intrusion depth is already reached at 3 µm. In contrast, the c-PSD analyses and the r_{max} are more strongly affected by the local heterogeneities. Hence, for the present example with local crack and heterogeneous porosity a relatively large sample volume is required for representative c-PSD analysis (i.e. critical thickness for c-PSD > 6 µm, whereas ID_{crit} for MIP-PSD is only 3 µm).

For the pore structure in the cathode (see Fig. 7b), the r_{50} from MIP-PSD (constricted) is only slightly smaller than the r_{50} from c-PSD (non-constricted). Both measurements are affected by the heterogeneous distribution of porosity. The r_{min} and r_{max} increase in a similar extent with increasing thickness, which is related to a higher porosity at the backside of the cube. However, as the ratio r_{min}/r_{max} remains

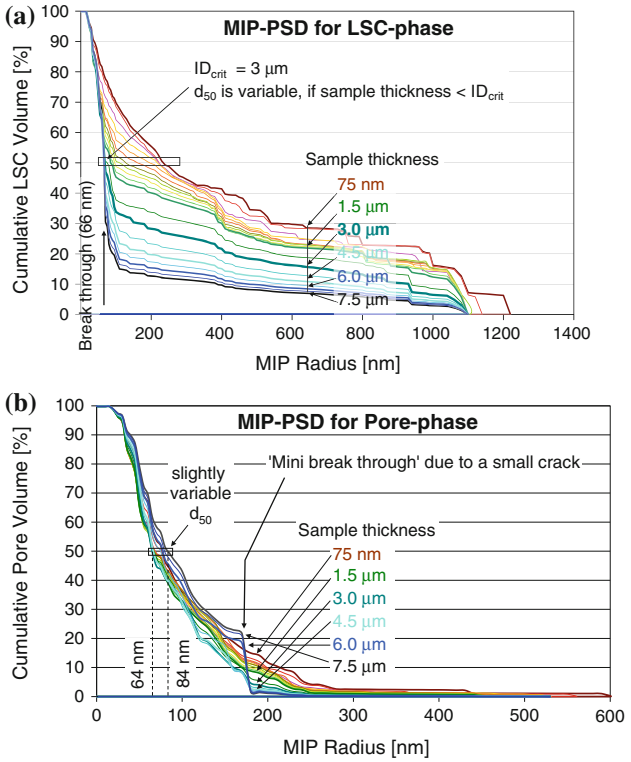

Fig. 6 MIP-PSD-curves for LSC (**a**) and pores (**b**). The MIP-simulations are performed repeatedly on data cubes from FIB-tomography, whereby the thickness of the cube is increased in steps of 75 nm up to 1.5 µm thickness, and then in steps of 1.25 µm up to 7.6 µm thickness. For the LSC-phase (**a**), the bottleneck effect becomes more pronounced with increasing thickness. The critical intrusion depth (ID_{crit}) is 3 µm. At larger sample thicknesses, the r_{50} radius is stable at 66 nm (i.e. r_{min}). For smaller sample thicknesses r_{50} is variable. The MIP-PSDs for the pore-phase (**b**) are less strongly affected by constrictions and hence they do not change significantly with increasing sample thickness. However, a small crack on the backside of the cube leads to a 'mini break through' at an intrusion depth of 5 µm

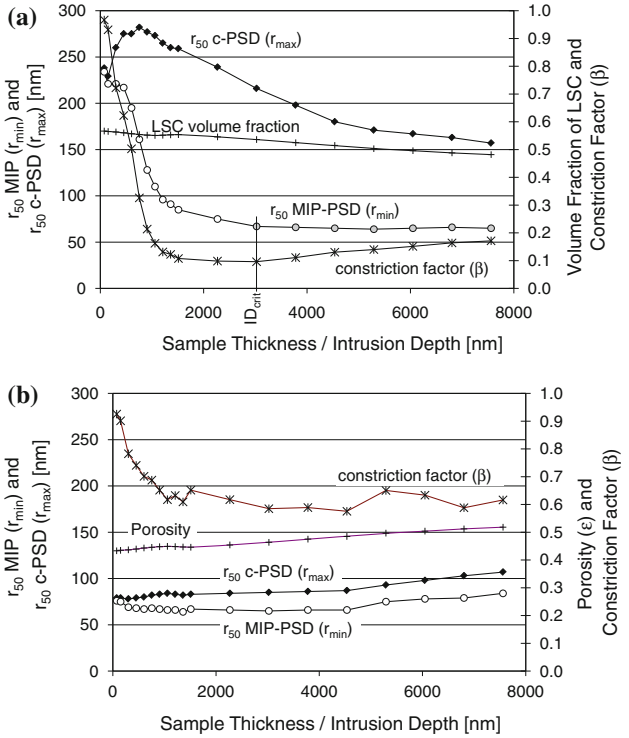

Fig. 7 Variation of r_{min} (from MIP) and r_{max} (from c-PSD) as a function of the sample thickness for the LSC-phase (**a**) and for the pore-phase (**b**) in a SOFC cathode. It is important to note that the volume fraction of pore is changing from 0.43 to 0.53 with increasing sample thickness due to a heterogeneous composition. r_{min} and the constriction factor (β) approach a plateau-value if the sample thicknesses is larger than ID_{crit} (at 3 µm). However, variable volume factions and a local crack 'destabilize' the plateau. The influence of these local heterogeneities on the constriction factors for pore and LSC-phases is discussed in the text

nearly constant, the constriction factor (β) also has a constant value of 0.6 ± 0.05. The results from the pore structure thus indicate that in microstructures with a weak constriction effect, local heterogeneities are affecting both the c-PSD and the MIP-PSD-measurements in a similar way. In spite of the heterogeneities, a stable and reproducible constriction factor can be obtained, as long as their effect is similar for both c-PSD and MIP measurements. It should be emphasized explicitly, that a local crack in the back part of the cube hardly affects the MIP-results, which is rather surprising.

Influence of different intrusion directions on MIP-PSD and r_{min}

The previous description of the porous LSC cathodes illustrates that the microstructure contains local heterogeneities (i.e. cracks, variation of solid and pore volume fractions, singularity of a very large particle). In this context, the question arises of whether different intrusion directions will lead to different results for the MIP-simulation due to those local heterogeneities. In order to test possible artificial anisotropy effects the intrusion is simulated for all six spatial directions. The resulting MIP-PSDs for the porous LSC cathode (compare Figs. 3 and 5) are plotted in Fig. 8. For the analyses of LSC, the six PSD-curves are nearly identical in the range where the cumulative volume is larger than 30 vol.%. Hence, the r_{50} of 64 (±1) nm is captured with a very good reproducibility, independently from the intrusion direction. In a similar way, MIP-PSDs of the pore-phase also give nearly the same r_{50} (84 ± 1 nm) for all six directions. Overall, the results indicate that the r_{min} can be extracted from MIP-PSDs with a very good reproducibility independent from the intrusion direction and in spite of the local heterogeneities.

Analysis of MIP-PSDs at the outlet-face (MIP-out)

The investigations with variable sample thickness show that the MIP-PSDs are instable at short intrusion depths. Even when the thickness is relatively large, the contribution of the analysed volume close to the entrance face (below ID_{crit})

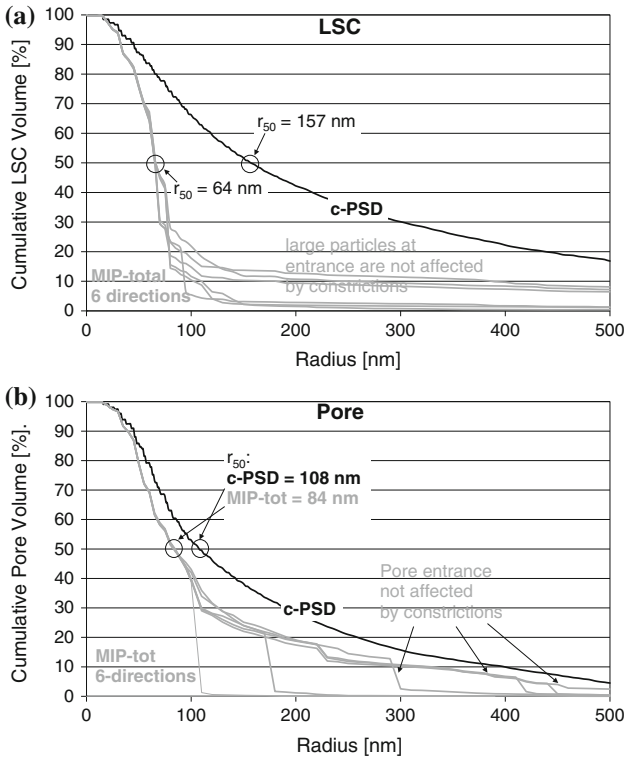

Fig. 8 MIP-PSDs (*grey*) for six different intrusion directions in a porous LSC cathode and comparison with the corresponding c-PSD (*black*). The PSDs are measured for the LSC-phase (**a**) and for the pore-phase (**b**). Note the perfect reproducibility of the r_{50} MIP (i.e. r_{min}) for all six directions of the intrusion

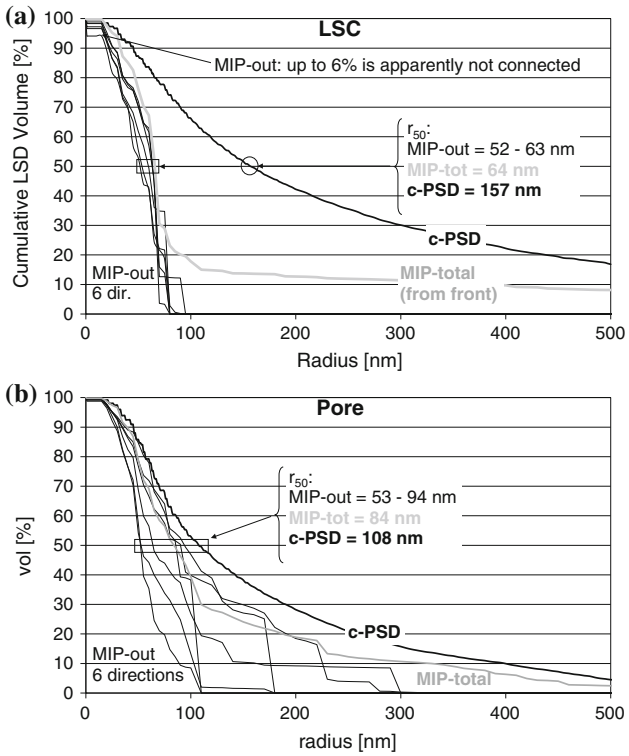

Fig. 9 PSD-curves representing the distribution of MIP radii in the outlet plane (MIP-out). The MIP-simulations are performed for six different intrusion directions based on a FIB-tomograph from a porous LSC cathode. PSDs are shown for the LSC-phase (**a**) and for the pores (**b**). A MIP analysis representing the PSD of the total sample volume (MIP-total, *bold grey curve*), and the corresponding c-PSD are also shown for comparison

leads to some variations in the PSD-curves, especially for the range of the PSD with the largest radii (see Fig. 8). An alternative way to use results from MIP-simulations is the restriction of the PSD analysis to the size information at the outlet-face. In this way, the MIP analysis excludes the volume at short intrusion distances (i.e. non-constricted domains at the entrance). This kind of MIP-PSD is subsequently called MIP-out, in contrast to the normal MIP-simulation of the total sample volume, which is called MIP-total. In Fig. 9, the MIP-out PSDs are shown for all six intrusion directions and they are compared with one PSD representing the typical MIP-total. The advantage of the MIP-out is that the deviations related to large non-constricted objects are no longer present. However, due to the small volume (actually only a 2D-slice), which is analysed, the reproducibility of the MIP-out PSD-curves is worse than those of the MIP-total (Fig. 8). Especially in the case where the bottleneck effect is less pronounced, the resulting size distributions from the outlet plane are not representative. Therefore, the r_{50} values extracted from MIP-out-PSDs of six different intrusion directions spread over a relatively wide range (53–94 nm). One could expect more precise results from MIP-out than from MIP-total, because problems related to short intrusion distances are suppressed. However, the area of single outlet-planes in MIP-out is too small and does not lead to a representative analysis. Larger imaging planes from FIB-tomography would be required to improve the statistical basis of MIP-out (Fig. 9), and thus MIP-total (Fig. 8) is currently more reliable.

Analysis of MIP-PSDs at the inlet face (MIP-in)

At short intrusion depths, the MIP radii are not yet dominated by the constrictions and, therefore, one can expect that the MIP-PSD from the inlet plane (subsequently called MIP-in) reveals the non-constricted dimensions of the particles or pores, respectively. Also the c-PSD is dominated by the size of the bulges and it is insensitive to the bottleneck effect. Therefore, the question arises whether MIP-in (pseudo-2D) or whether c-PSD (3D) should be used for the determination of r_{max}?

The MIP-in PSDs are shown in Fig. 10 for all six directions of intrusion. The single MIP-in PSDs are quite different from each other. However, if the six analyses are averaged (grey bold curve) then this curve is nearly identical to the c-PSD curve that is obtained from the total

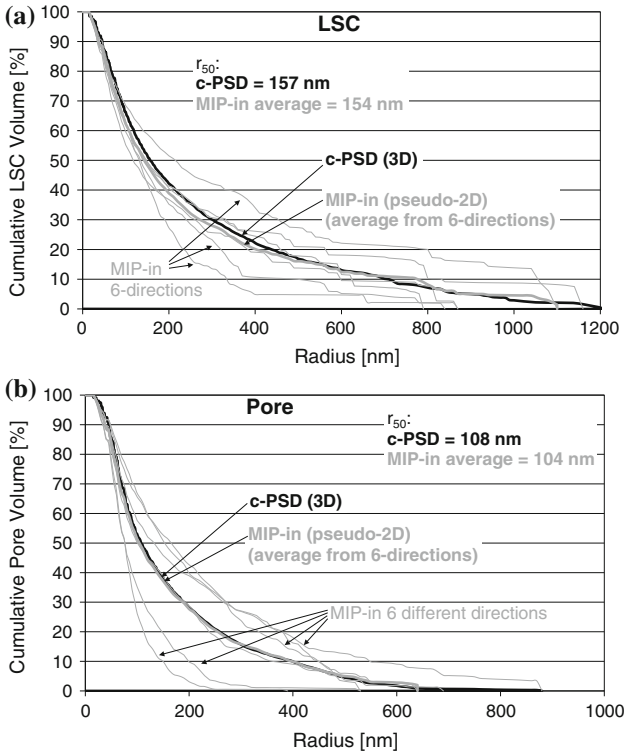

Fig. 10 MIP-PSD-curves measured only from the inlet-planes (i.e. MIP-in). Results are shown for LSC (**a**) and for pores (**b**). The MIP-in PSDs are performed for six different intrusion directions from a FIB cube of a porous LSC cathode. The large variation is attributed to statistical problems caused by the relatively small area of the inlet-planes. The average PSD curve includes all six MIP-in analyses (*bold grey*) and it is nearly identical with the c-PSD curve from the total FIB volume (*bold black*)

volume. The same behaviour is observed for LSC (a) and for pores (b). The variations of the MIP-in PSDs can be attributed to the fact that the inlet-planes are not large enough to capture the wide particle size distribution in a representative way. Hence, if the analysed volume is large enough to give representative results, then the MIP-in and the c-PSD are identical and both methods reveal the same r_{max}. Obviously, the c-PSD, which is performed in 3D from the entire data cube, has a better statistical basis than the PSDs from MIP-in, which are obtained only from the 2D inlet-planes at the cube surfaces. These results strongly support the use of c-PSD (instead of MIP-in) for the determination of the r_{max}, which is then used for the calculation of the constriction factor (β).

Quantitative relationship between β and δ: investigation of porous diaphragms

From the previous section it follows that the constriction factor (β) is a microstructure parameter, which is entirely defined by measurable geometrical features (i.e. r_{min} and r_{max}). However, its relationship with the macroscopic transport properties in complex microstructures is so far not established. In contrast, constrictivity (δ) is a parameter, which can be determined based on experiments that deliver the effective transport properties (see Eq. 3). Constrictivity (δ) is thus measured indirectly and it is not based on any morphological analysis of the microstructure. Consequently, there is a need to establish a quantitative relationship between the constriction factor (β) and the constrictivity (δ), whereby the first parameter relates to the microscopic geometry and the second parameter relates to the experimentally measured transport properties.

In this article, we intend to establish such a relationship based on experimental data from porous diaphragms. The effect of the pore structure on ion conductivity in olivine and in wollastonite diaphragms was investigated in a previous study of Wiedenmann et al. [37] by means of EIS and SRμCT. Under the view that new possibilities for measuring the constriction factor (β) are available, we re-evaluate the experimental data from the previous study.

The main findings of the previous study [37] can be summarized as follows: the effective ion conductivities (see Fig. 11), which are measured with EIS, increase exponentially with porosity. The two materials define separate trends for porosities between 0.25 and 0.8. According to Archie's law characteristic exponential *m*-factors can be determined empirically, whereby *m* is 2.95 for the olivine- and 2.31 for the wollastonite diaphragms. The empirical descriptions with *m*-factors do not explain which morphological features are controlling the transport properties.

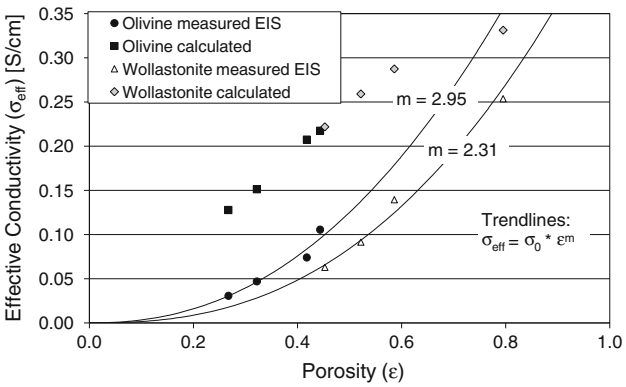

Fig. 11 Effective ion conductivities (σ_{eff}, measured and calculated) versus porosity in olivine and wollastonite diaphragms (data from Wiedenmann et al. [37]). The measured ion conductivities (*black circles* and *open triangles*) are determined with 4-point EIS. The calculated conductivities (*black squares* and *grey rhombi*) are obtained by substitution of ε, τ_{geo} (both obtained from tomography and image analysis) and σ_0 into Eq. 2. *Note* the measured conductivities follow two different exponential trends, which are compatible with Archie's law. In contrast, the calculated conductivities are significantly higher than the measured conductivities. In the calculated conductivities, the effect of bottlenecks is not considered. Hence, the different results illustrate the importance of the constrictivity

According to conventional transport models, it was expected that tortuosity is the main morphological parameter which dominates the transport properties of the two materials series. Surprisingly, however, the geometric tortuosities of both materials series do not vary significantly with changing porosity. The geometric tortuosities, which are determined from the tomographs, can be used to calculate the effective conductivities. For this purpose, τ_{geo}, ε and σ_0 are substituted in Eq. 2. The calculated effective conductivities of the two materials series define a single trend line (see calculated σ_{eff} in Fig. 11), which is very different from the experimentally measured conductivities. This result indicates that the geometric tortuosities do not fully capture the morphological features, which are relevant for the transport properties. As shown in Fig. 12, the geometric tortuosities (τ_{geo}) for both materials series are nearly constant with an average value of 1.62. Figure 12 also shows the so-called experimental or electrical tortuosities (τ_{elc}), which are determined indirectly by resolving Eq. 2 for τ. Thereby, unrealistically high values up to 5.6 are obtained for τ_{elc}. It is assumed that the high values for the electrical tortuosity do not signify such long pore pathways, but instead are caused by artefacts related to the indirect determination procedure. Other geometric features such as the constrictivity may be included in the electrical tortuosity, which leads to the high τ_{elc} values. Hence, the results from porous diaphragms indicate that the real pore path lengths (which are described by τ_{geo}) are not the main microstructure feature, which influences effective transport properties. Constrictivity is considered as an additional microstructure feature, which may be more critical for transport in the porous diaphragms than τ_{geo}. Using MIP and c-PSD analyses, a more detailed description of the pore structure including the constriction effect can now be introduced.

The radii r_{min} from MIP-PSD and r_{max} from c-PSD are plotted in Fig. 13. Linear trends in this diagram represent constant β values (since $\beta = r_{min}^2/r_{max}^2$). The measured data points are best fitted with a slightly nonlinear trend line, which indicates that β is increasing with larger pore sizes. As shown in Fig. 14, β also correlates positively with porosity, which indicates that the bottleneck effect becomes more pronounced in samples with smaller porosity. Furthermore, the data points in Fig. 14 do not define a clear single trend line. Obviously, the different particle shapes of olivine (spheroid) and wollastonite (fibrous) also lead to different bottleneck geometries and associated constrictivities.

Using the experimental data (σ_{eff}, τ_{geo}, ε), constrictivity can be calculated as follows:

$$\delta = \frac{\sigma_0 \tau_{geo}}{\sigma_{eff} \varepsilon} \tag{8}$$

The thus derived constrictivity (δ) is plotted versus the measured constriction factor (β) in Fig. 15. Based on these data, we define an empirical relationship between the two parameters. In the β range from 0.4 to 0.6, the data points indicate a trend with a slope that is steeper than the diagonal (where $\beta = \delta$). For extreme values of β, the following 'boundary conditions' can be assumed: (a) for $\beta = 1$, $\delta = 1$. This describes the case where the pores have

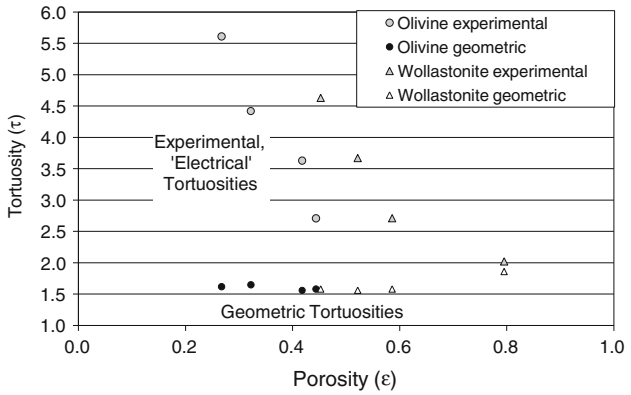

Fig. 12 Geometric and electrical tortuosities from olivine and wollastonite diaphragms plotted versus the corresponding porosity (data from [37]). The geometric tortuosity (τ_{geo}), which is obtained by image analysis directly from tomographs, hardly changes with porosity. The average τ_{geo} is 1.62. In contrast, the electrical tortuosity (τ_{elc}), which is calculated indirectly using the effective conductivity (σ_{eff}) from EIS, shows unrealistically high values up to 5.6. The reason for this difference is that the experimental tortuosity erroneously includes the effect of bottlenecks, whereas the geometric tortuosity strictly only describes the pore paths lengths

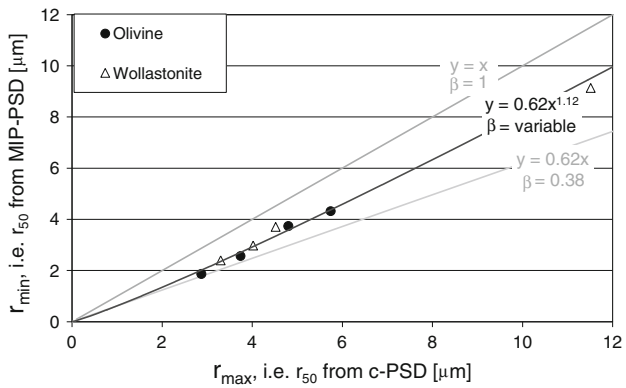

Fig. 13 Plot of pore radii r_{min} versus r_{max} in wollastonite and olivine diaphragms. The r_{min} from MIP-PSD is interpreted as a characteristic measure for the dimension of the pore necks. The r_{max} from c-PSD reflects the average size of the non-constricted pore bulges. The *grey lines* define trends with constant β (since $\beta = r_{min}^2/r_{max}^2$). The measured data points, however, are better fitted with a nonlinear trend (*black*), which indicates that the β values are increasing with pore size

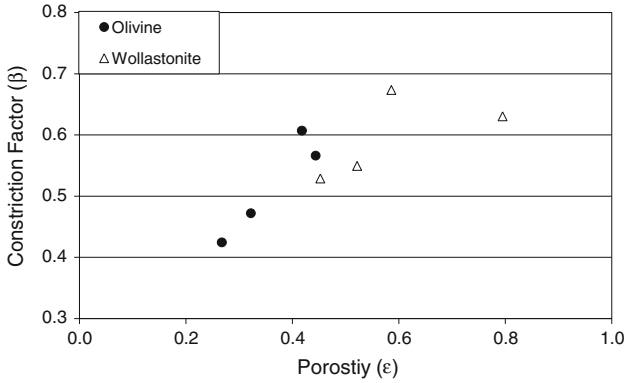

Fig. 14 Plot of constriction factor (β) versus porosity (ε) in diaphragms made of wollastonite (*filled circles*) and olivine (*open triangles*). With decreasing porosity the constriction effect becomes stronger (i.e. β is decreasing). In addition, the data points from olivine and wollastonite do not define a clear, single trend line. It is assumed that the different grain shapes in the two materials (olivine and wollastonite) lead to measurable differences of the pore neck dimensions and associated constriction factors

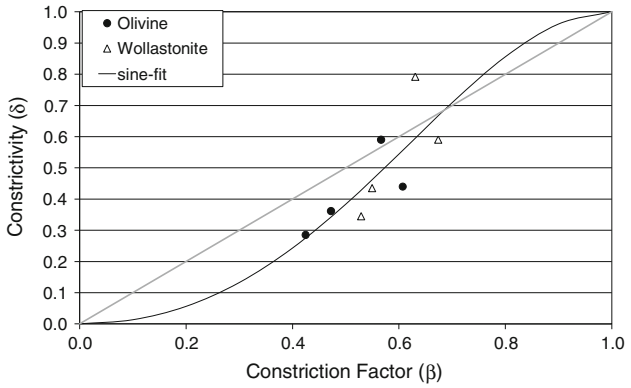

Fig. 15 Plot of constrictivity (δ) versus constriction factor (β) for porous diaphragms of olivine (*filled circles*) and wollastonite (*open triangles*). The constriction factor (β) is geometrically well-defined (r^2_{min}/r^2_{max}) and it is directly measured from tomographs. The constrictivity (δ) is calculated indirectly, using experimental data from EIS and τ_{geo}. The data points are used to define a quantitative relationship between β and δ which has the form of a sine-function (see Eq. 9)

no constrictions (e.g. pores form straight pipes) and (b) for $\beta = 0$, $\delta = 0$. This represents the case where the necks fully close the pore pathways (i.e. loss of connectivity). The data points in Fig. 15 (steep slope for intermediate β-range) with boundary conditions of 0,0 and 1,1 can then be fitted with a sine curve according to the following empirical equation:

$$\delta_{geo} = \frac{\left[\mathrm{Sin}\left((\pi\gamma) + \frac{\pi}{2}\right)\right]}{2} + \frac{1}{2}. \quad (9)$$

Thereby γ is a quadratic function of β, with $a = 0.3$, $b = 0.7$ and $c = 0$

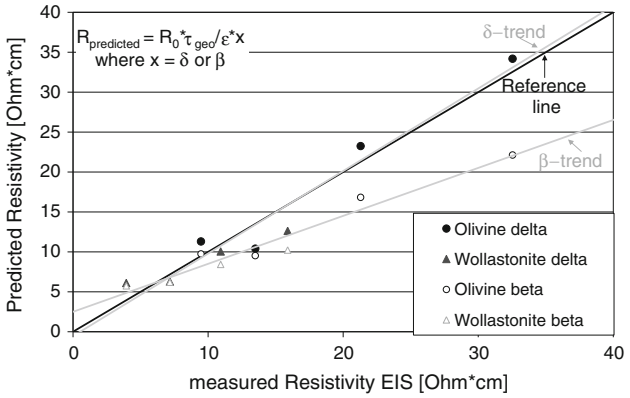

Fig. 16 Predicted resistivities (y-axis, using Eqs. 9–11) are plotted against the corresponding measured resistivities (x-axis). The measured resistivities are obtained with EIS [37]. The calculation of the predicted resistivities is based on microstructure parameters that are measured from tomographs by means of 3D-image analysis. Thereby, the predictions based on δ (*black*, *filled symbols*) show a better match with the measured resistivity (i.e. *black reference line*) than the predictions based on β (*open symbols*)

$$\gamma = a\beta^2 + b\beta + c. \quad (10)$$

Using Eqs. 9 and 10, the geometrical constrictivity (δ_{geo}) can now be determined based on data from microstructure analysis (i.e. β, r_{min}, r_{max}). Furthermore, the effective transport properties (i.e. resistance for ion conduction, R_{eff}) can now also be predicted based on data, which is entirely derived from microscopic investigations, according to the following expression:

$$R_{eff} = \frac{R_0 \tau_{geo}}{\varepsilon\, \delta_{geo}} \quad (11)$$

In Fig. 16, the predicted resistivities (using Eqs. 9–11) are plotted versus the measured resistivities from EIS. The data points, which are obtained using δ_{geo} (black filled symbols), nicely follow the diagonal line (i.e. they match the measured resistivities). For comparison, predicted resistivities are also calculated by simply substituting the constriction factor (β) into Eq. 11, instead of constrictivity (δ_{geo}). The resulting data points (white open symbols) are plotting below the diagonal line, which indicates that the true resistivity is underestimated when predictions are based simply on the constriction factor (β). Nevertheless, at small resistivities the difference between predictions using β and or δ_{geo} is not large. If conductivity is investigated instead of resistivity, then the difference between the two predictions becomes even smaller (as shown in [37]).

Conclusions

The geometrical tests with porous LSC-cathodes confirm the first hypothesis of this paper, according to which

MIP-PSD can be used to determine the characteristic dimensions of the bottlenecks (r_{min}). The tests show that MIP-PSD is insensitive to the intrusion direction and also to the presence of local heterogeneities (cracks, single large objects), as long as the thickness of the analysed sample is larger than the critical intrusion depth (ID_{crit}). For granular materials, ID_{crit} is approximately 2–5 times the radius of the largest particles.

The geometrical tests also confirm the second hypothesis, according to which the c-PSD can be used to characterize the typical dimensions of non-constricted bulges (i.e. r_{max}). However, c-PSD is more sensitive to local heterogeneities and structural gradients (e.g. changing pore and solid volume fractions). Therefore, a larger sample volume must be analysed (compared to MIP-PSD) to obtain a statistically representative and stable result.

Using r_{min} and r_{max}, the constriction factor (β) can now be extracted directly from tomographs of complex microstructures, which was the third hypothesis. Thereby, the constriction factor appears to be positively correlated with porosity and with pore size, which indicates that the bottleneck effect is stronger in low porosity materials and in fine-grained microstructures.

Using experimental data from EIS the constrictivity (δ) could be calculated indirectly for diaphragm samples with different pore sizes. According to the fourth hypothesis, an empirical relationship can then be established between the geometrical constriction factor (β) and the experimental constrictivity (δ). According to our data, this empirical relationship has the form of a sine-function (Eqs. 9 and 10).

The fifth and last hypothesis of this study states that the effective transport properties on a macroscopic scale can be predicted based on the volume averaged parameters from tomography (ε, r_{min}, r_{max}, β, τ_{geo}) and by taking into account the empirical relationship between β and δ. In this study, the effective transport properties for wollastonite and olivine diaphragms can be predicted in this way. Nevertheless, future studies will have to show for which types of materials, for which range of porosities and for which transport mechanisms (diffusion, conduction, flow) the fifth hypothesis is valid.

In section 'Introduction', we have emphasized that the prediction of transport properties based on volume averaged parameters is no more than a heuristic approximation to a more complex problem. Nevertheless, the results of this study deliver a solid methodological basis for such heuristic transport predictions. The strength of the heuristic approach is the fact that the (now measurable) underlying parameters help to understand in which way the microstructure can be optimized in materials with structural transport limitations (e.g. in porous membranes for electrolysis cells or in porous electrodes for SOFC).

Acknowledgements L.H. would like to thank Thomas Hocker (ZHAW) for fruitful discussions about modelling of transport processes. Andre Hell is acknowledged for preparation of the LSC-powders by flame spray synthesis.

References

1. Kozeny J (1927) Wien 136a:271
2. Carman PC (1956) Flow of gases through porous media. Butterworths, London
3. Archie GE (1942) Trans AIME 146:54
4. Sahimi M (ed) (1995) Flow and transport in porous media and fractured rock. VCH, Weinheim
5. Bird RB, Stewart WE, Lightfoot EN (eds) (2007) Transport phenomena, 2nd edn. Wiley, New York
6. Ohser J, Mücklich F (2000) Statistical analysis of microstructures in materials science. Wiley, Chichester
7. Salem HS, Chilingarian GV (2000) Energy Sour A 22:137
8. Wilson JR, Kobsiriphat W, Mendoza R et al (2006) Nat Mater 5:541. doi:10.1038/nmat1668
9. Holzer L, Iwanschitz B, Hocker T et al (2011) J Power Sources 196:1279
10. Holzer L, Münch B, Iwanschitz B, Cantoni M, Hocker T, Graule T (2011) J Power Sources 196:7076
11. Thiedmann R, Hassfeld H, Stenzel O et al (2011) Image Anal Stereol 30:19
12. Shearing PR, Howard LE, Jorgensen PS, Brandon NP, Harris SJ (2010) Electrochem Commun 12:374
13. Mader K, Marone F, Hintermuller C, Mikuljan G, Isenegger A, Stampanoni M (2011) J Synchrotron Radiat 18:117
14. Holzer L, Indutnyi F, Gasser P, Münch B, Wegmann M (2004) J Microsc 216:84
15. Holzer L, Cantoni M (2012) In: Utke I, Moshkalev SA, Russell P (eds) Nanofabrication using focused ion and electron beams: principles and applications. Oxford University Press, New York
16. Shaikjee A, Franklyn PJ, Coville NJ (2011) Carbon 49:2950
17. Lopez-Barron CR, Macosko CW (2011) J Microsc 242:242
18. Thiedmann R, Hartnig C, Manke I, Schmidt V, Lehnert W (2009) J Electrochem Soc 156:B1339
19. Keller LM, Holzer L, Wepf R, Gasser P (2011) Appl Clay Sci 52:85
20. Münch B, Holzer L (2008) J Am Ceram Soc 91:4059
21. Clennell MB (1997) In: Lovell MA, Harvey PK (eds) Developments in petrophysics. Geological Society Special Publication, London
22. Bhatia SK (1985) J Catal 93:192
23. Lindquist WB, Lee SM, Coker DA, Jones KW, Spanne P (1996) J Geophys Res 101:8297
24. Hirsch LM, Schuette JF (1999) Comput Geosci 25:127
25. Boudreau BP (1996) Geochim Cosmochim Acta 60:3139
26. Shen L, Chen Z (2007) Chem Eng Sci 62:3748
27. Satterfield CN, Cadle PJ (1968) Ind Eng Chem Process Des Dev 7:256
28. Katsube TJ, Modford BS, Best ME (1991) Geophysics 56:1681
29. Van Brakel J, Heertjes PM (1974) Int J Heat Mass Transfer 17:1093
30. Petersen EE (1958) AIChE J 4:343
31. Michaels AS (1959) AIChE J 5:270
32. Prestat M, Morandi A, Heel A, Holzer L, Holtappels P, Graule T (2010) Electrochem Commun 12:292
33. Heel A, Holtappels P, Graule T (2010) J Power Sources 195:6709
34. Holzer L, Münch B, Wegmann M, Flatt R, Gasser P (2006) J Am Ceram Soc 89:2577
35. Holzer L, Münch B (2009) Microsc Microanal 15:130

36. Holzer L, Muench B, Rizzi M, Wepf R, Marschall P (2010) Appl Clay Sci 47:330
37. D Wiedenmann, L Keller, L Holzer, et al. (2012) AIChE J (in press)
38. Sato M, Bitter I, Bender M, Kaufmann AE (2000) In: Barsky BA, Shinagawa J, Wang W (eds) 8th Pacific conference on computer graphics and applications. IEEE Computer Society, Washington, DC
39. Jungnickel D (1999) Graphs, networks and algorithms. Springer, Berlin
40. Cormen TH, Leiserson CE, Rivest RL, Stein C (2009) Introduction to algorithms, 3rd edn. MIP Press, Cambridge
41. Keller LM, Holzer L, Wepf R, Gasser P, Münch B, Marschall P (2011) Phys Chem Earth 36:1539
42. Washburn EW (1921) Proc Natl Acad Sci USA 7:115
43. Washburn EW (1921) Phys Rev 17:273
44. Diamond S (2000) Cem Concr Res 30:1517